Imaging Quantum Vortices in Superfluid Helium Droplets

Oliver Gessner[1*] and Andrey F. Vilesov[2,3*]

[1] Chemical Sciences Division, Lawrence Berkeley National Laboratory, Berkeley, California 94720, USA

[2] Department of Chemistry, University of Southern California, Los Angeles, California 90089, USA

[3] Department of Physics and Astronomy, University of Southern California, Los Angeles, California 90089, USA

Abstract

Free superfluid helium droplets constitute a versatile medium for diverse experiments in physics and chemistry that range from studies of the fundamental laws of superfluid motion to the synthesis of novel nanomaterials. In particular, the emergence of quantum vortices in rotating helium droplets is one of the most dramatic hallmarks of superfluidity and gives detailed access to the wavefunction describing the quantum liquid. This review provides an account of recent advances in studying the rotational motion of isolated, nano- to micron-scale superfluid helium droplets. Especially, ultrafast X-ray and XUV scattering techniques enabled by X-ray free electron lasers and high-order harmonic generation have facilitated the *in situ* detection of droplet shapes and the imaging of vortex structures inside individual, isolated droplets. New applications of the "cryogenic nanolabs" are discussed that may range from studies of quantum phase separations to mechanisms of low temperature aggregation.

Keywords: helium nano-droplets, superfluidity in 4-He, quantum vortices, X-ray coherent diffraction imaging, free electron lasers.

[*] corresponding authors: ogessner@lbl.gov, vilesov@usc.edu

1.Introduction

Free superfluid helium droplets constitute a versatile medium for a diverse range of experiments in physics and chemistry. Following an Annual Review in Physical Chemistry article two decades ago (1), research involving He droplets has been highlighted in a number of reviews. (2-18) In many applications, He droplets serve as an ultracold matrix for spectroscopic interrogation of single molecules, radicals and ionic species. In addition, clusters may be readily prepared inside droplets upon sequential capture of single atoms and molecules. Low temperatures of about 0.4 K (19; 20) in combination with the weak interaction of dopants with the homogeneous quantum liquid environment result in very narrow spectral lines. Embedded single molecules also provide a unique local probe for superfluidity on an atomic length scale, which has been studied via renormalization of molecular rotational constants. (19-22) The coupling of molecular rotors to the helium bath has also been probed via adiabatic and impulsive alignment of dopant molecules in strong laser fields, (23-25) whereby the encapsulation in He droplets enabled a higher degree of alignment than in free molecules (26).

More recently, superfluid droplets have emerged as unique nano-laboratories for the study of quantum effects in finite isolated systems. Below the critical temperature of T_λ = 2.17 K, ^{4}He enters the superfluid phase (often referred to as He II) that lacks any viscosity, and its motion is described by a wavefunction (27-31). Non-rotating superfluid droplets have a spherical shape. A rotating droplet, however, is deformed due to centrifugal forces and stores its angular momentum in the form of one or multiple quantum vortices (29-31). Droplet shapes and the vortex configurations they contain provide the most complete characterization of the macroscopic wave function of a superfluid droplet. Imaging vortices, however, is challenging due to their extremely small core diameters of only ~2 Å. It is commonly facilitated by doping droplets with foreign particles that coalesce near the vortex cores by hydrodynamic forces (32-34). The particles either serve as “contrast agents” for *in situ* imaging or are deposited on substrates and imaged *ex situ*. This paper reviews experiments on vortex visualization in bulk superfluid He and, in particular, recent advances in imaging quantum vortices in sub-micrometer sized He droplets. The latter

has become possible by *ex situ* transmission electron microscopy (TEM) and ultrafast *in situ* x-ray scattering using X-ray free electron lasers (XFELs) and femtosecond high-order harmonic generation (HHG) light sources.

This article starts with a brief introduction into the vorticity in superfluid helium followed by an overview on detecting and tracing quantum vortices in bulk He II. Moving to microscopic, self-contained systems, we discuss the shapes of rotating classical and superfluid droplets and the *ex situ* tracing of quantum vortices in He droplets by electron microscopy of deposits left behind after doped droplets impact on a substrate. Three sections are dedicated to the latest developments of *in situ* detection and imaging of shapes and vorticities of free helium nanodroplets by ultrafast X-ray scattering. Section 6 introduces the technique and describes the detection of droplet shapes and vortex lattices. Section 7 details the coherent diffraction imaging of few vortex configurations in individual He droplets by a droplet-assisted phase reconstruction technique that determines the structure of dopant clusters. This is followed by a discussion of the impact of doping on the vortex kinematics, which turns out to be significant in many cases and needs to be taken into account when comparing measured and predicted vortex configurations. Finally, we summarize and give an outlook toward some of the scientific opportunities that arise from the techniques presented in this work.

2.Quantum vortices in superfluid ^{4}He droplets

Quantum vortices are among the most dramatic hallmarks of superfluidity (28; 30; 31; 35). In contrast to a normal fluid, which rotates as a rigid body with the same angular velocity ω as its container, a superfluid will remain at rest for small values of ω. Above a certain critical ω, however, the thermodynamically stable state of the superfluid includes one or more quantum vortices (36; 37). At a fixed angular velocity, such as in a rotating bucket experiment, the equilibrium is given by minimizing the free energy in the rotating frame (36; 38). In the case of a free droplet with a constant angular momentum, the

equilibrium is defined by the minimum of the free energy in the laboratory frame (36). A quantum vortex has a quantized velocity circulation in units of $\kappa=h/M=9.97\times10^{-8}$ $m^2\cdot s^{-1}$, where h is Planck's constant and M is the mass of the ^{4}He atom. (30; 31) Free vortices with multiple κ quanta are unstable with respect to dissociation into several singly quantized vortices.(30; 31) Due to centrifugal effects, the density of liquid helium in the vortex core is depleted (39; 40). In the absence of any experimentally determined density profiles, the core region of quantum vortices is often represented as a cylindrical void with a radius ξ= 0.1 nm (30; 41). Within this so-called hollow core model, a rectilinear vortex passing through the center of a cylinder with length l and radius R (or a spherical vessel or a droplet with radius R), has an energy of (36; 37)

$$E_{cyl} = \frac{\kappa^2\cdot\rho_0\cdot l}{4\cdot\pi}\cdot\ln\left(\frac{R}{\xi}\right) \qquad (2.1)$$

$$E_{sph} = \frac{\kappa^2\cdot\rho_0\cdot R}{2\cdot\pi}\cdot\left(\ln\left(\frac{2\cdot R}{\xi}\right)-1\right) \qquad (2.2)$$

Here, ρ_0 = 145 $kg\cdot m^{-3}$ is the density of liquid helium at low temperature (42). The angular momentum per He atom of a rectilinear quantum vortex is $\hbar=h/2\pi$.

The local velocity in the superfluid, $v(r)$, of constant density is given by the gradient of the phase of the macroscopic wave function, S, as (28; 30; 31)

$$v(r) = \frac{\hbar}{M}\nabla S(r)\ . \qquad (2.3)$$

For a vortex with a single unit of circulation the phase winds by 2π around the vortex core. As a result, the velocity at a distance r from the core of a singly quantized rectilinear vortex is tangential with an absolute value of:

$$v(r) = \frac{\kappa}{2\pi\cdot r} \qquad (2.4)$$

If the total angular momentum in the quantum liquid is less than $\hbar$ per atom, a vortex at some distance away from the rotational axis may be formed (38). Each vortex must terminate perpendicular to the liquid's boundary to ensure zero flux through the surface. Therefore, non-central vortices in droplets are curved and carry a smaller amount of energy than central, rectilinear vortices (36; 37; 43). Note that curved vortices are not stationary but rotate around the fluid's rotational axis.

Eqs. (1-4) show that away from the core region, the kinetic energy per unit volume of the liquid changes as $\propto 1/r^2$. A foreign particle displaces liquid and thus reduces the total kinetic energy of the fluid. The net effect is the attraction of a particle toward the vortex core, which can also be interpreted as an effect of Bernoulli forces resulting from the velocity gradient in eq.(2.4) (34). The effective particle binding energies, as obtained by density functional theory (DFT) for a number of atoms and molecules, are on the order of a few Kelvin (39; 44). For example, the binding energy of Xe atoms was estimated between 3.2 K(45) and 5.0 K(39). Semiclassical matter wave calculations estimate an impact parameter of ≈0.5 nm for the capture of a Xe atom by a vortex (46). Recently, the capture dynamics of Ar and Xe atoms by He droplet vortices have been studied via TDFT calculations (47). The results of the calculations presented in Figure 2.1 reveal that upon impact, trapping of the particles is facilitated by energy dissipation through the creation of large amplitude deformations of the vortex core as well as helical Kelvin waves (30; 31) on the vortex core.

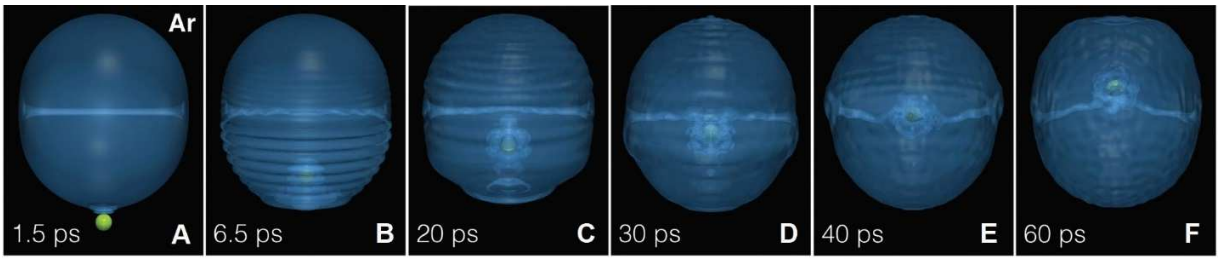

Fig. 2.1. Capture of Ar atom by a vortex in a ^{4}He droplet of 1000 atoms. A: An Ar atom (green dot) collides at 360 m/s with a droplet containing a single rectilinear vortex. B: The Ar atom penetrates into the droplet, inducing density waves. C: A He solvation shell is built around the Ar atom. D: The Ar atom approaches the vortex. E: The Ar atoms reaches the vortex core and induces vortex distortion. F: The Ar atom is trapped by the vortex, which continues to oscillate. The time is indicated in each frame. Modified from (47).

Upon increase of the ω of a bucket filled with superfluid helium or of the angular momentum, *L*, of a superfluid droplet, thermodynamically stable configurations involve several quantum vortices. In the idealized case of a thin plane-parallel layer rotating at ω, vortices are predicted to form an equilateral triangular lattice (30), which may be viewed as a Wigner crystal with a lattice structure defined by the mutual repulsion of the vortices. The angular velocity ω can be obtained from the average vorticity as: (28)

$$\omega = \frac{n_V \cdot \kappa}{2} \quad , \qquad (2.5)$$

where n_V is the areal density of the vortices. The angular momentum of the system per He atom is $\hbar/2$ multiplied by the total number of vortices. Calculated configurations of multiple vortices in a cylinder resemble equilateral triangular patterns close to the center, but exhibit noticeable circular deformations toward larger radii (48). Analytic expressions for the free energy of symmetric arrangements of straight vortices in a cylinder (38) and a sphere (49) have been derived. The shapes and dynamics of bare vortices in a container with fixed boundary conditions can be calculated using the Biot-Savart law (50-53). The equilibrium corresponds to a vortex configuration that is stationary in a frame rotating at some ω. However, the implementation of this approach, which requires calculation of the vortex images, is only feasible for

simple geometries, such as in a square channel, a cylinder or a sphere (48; 50-53). Similar calculations for systems with free deformable surfaces, such as a droplet or for doped vortices have not yet been demonstrated.

Currently, DFT (16; 45) remains the only *ab initio* computational technique that yields the shapes of droplets and geometries of vortices therein as well as the phase of the wavefunction (related to the velocity field by eq. (2.3)) in a free droplet with a specific total angular momentum (43; 54). Fig. 2.2 shows calculated density of He droplets containing two to nine vortices. The vortex cores are marked by depleted densities, which are represented as black dots or curves along the direction of angular momentum and perpendicular to it, respectively. The vortices are stationary in the frame rotating with ω, which increases with the number of vortices. With increasing ω, the droplets become oblate and the vortex configurations become increasingly axially symmetric.

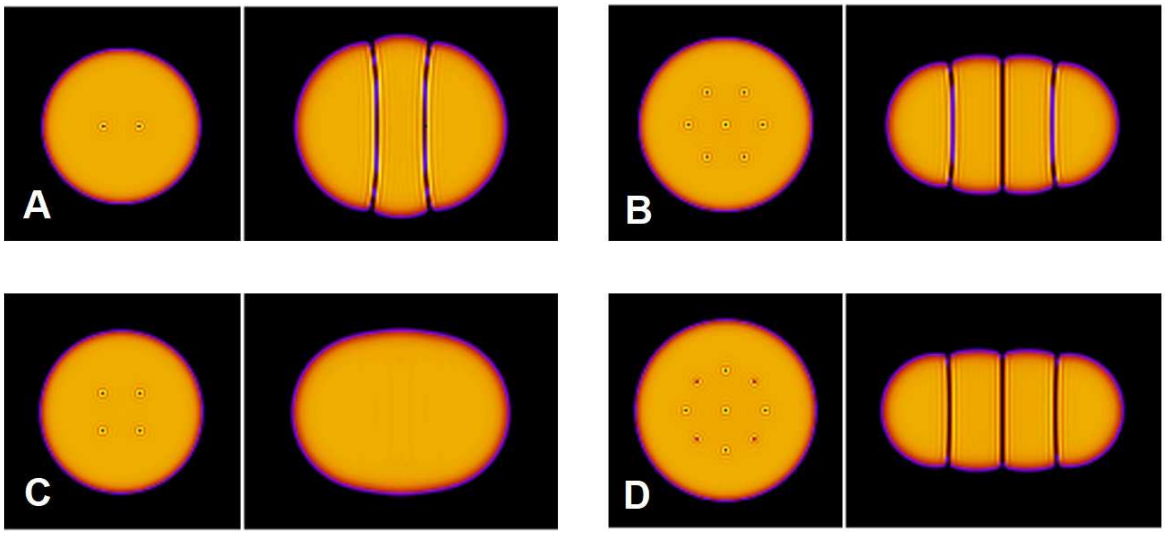

Fig. 2.2. Helium droplet containing 15000 atoms hosting 2, 4, 7, and 9 vortices in panels A, C, B and D, respectively. The images on the left and right in each panel show the density cross sections perpendicular to and along the direction of the angular momentum, respectively. The density is color coded from black to orange, corresponding to zero and bulk liquid density, respectively. Modified from Ref. (43).

3. Detection and Imaging of vortices in bulk ^{4}He

Various imaging techniques have been developed for visualizing vortices, all of which employ tagging of the vortex cores with impurities. Already the first experimental demonstration of quantized circulation by Vinen (35), later refined by Zimmermann and co-workers (55), used a variation of this idea. A vortex was attached to a micrometer-diameter, vibrating wire stretched along the center of a rotating bucket filled with He II. The presence of the vortex gave rise to a splitting of the otherwise degenerate vibrational modes of the wire due to the Magnus effect. It was also shown that multiply quantized vortices may be stabilized by the wire.(35; 55) While this technique provided pioneering results, it was extremely challenging and not suited to study free vortices.

In most of the later experiments, to allow for mobility, the vortices were doped with impurities such as electrons, neutral or ionized atoms, and larger particles such as hydrogen or metallic clusters. Early ion mobility measurements used ion scattering and trapping in vortices (56-59). Rayfield and Reif performed drift velocity measurements on positive and negative ions in He II with various kinetic energies (56). Low temperatures of 0.3-0.6 K ensured minimal scattering of the ions on thermal excitations. The astonishing finding was that the drift velocity was *inversely* proportional to the kinetic energy (56; 57), which led the authors to conclude that the ions were attached to free quantized vortex rings. The measurements led to the first and only experimental determination of the vortex core radius of ~0.1 nm (56; 57).

The first images of the geometric arrangements of several vortices inside rotating He II required extensive experimental developments by Packard and co-workers spanning about a decade (32; 61-63). They employed electrons to trace vortex configurations as illustrated in Fig. 3.1.a. (32). Due to Pauli repulsion, electrons in liquid He are surrounded by 3.4 nm diameter voids (“bubbles”) (64; 65), and are readily trapped by quantum vortices. The electrons were extracted from the liquid by an electric field aligned along the axis of rotation and accelerated toward a phosphor screen that was imaged onto a video camera. Fig. 3.1.b shows examples of patterns obtained at increasing ω, which are in qualitative agreement

with theoretical predictions (32; 38). For comparison, Fig. 3.1c shows the vortex pattern in a dilute, rotating BEC of sodium atoms held in a magnetic trap (60). Similar to He II, rotation of a BEC is also realized by the emergence of quantized vortices (28). The vortex patterns in the BEC are highly symmetric and exhibit triangular lattice structures as predicted by Abrikosov (66) and Tkachenko (67). Despite the evident similarities among Figs.3.1b,c, we note that BECs may often be viewed as quasi two-dimensional systems (31; 60; 68; 69). In comparison to dilute BECs held in traps, ^{4}He droplets are self-contained and represent a strongly interacting superfluid.

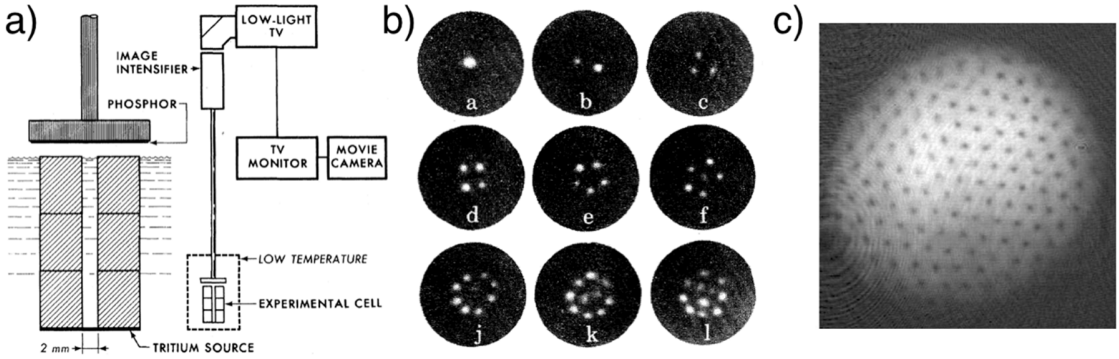

Figure 3.1: a) First imaging of vortices in in rotating He II (from (32)). A tritium source at the bottom is used to inject electrons that attach to the vortex cores. The electrons are extracted and accelerated onto a phosphor screen. The electron trajectories are stabilized by an axial 0.4 T magnetic field. The resulting pattern is transmitted to the electronic imaging system via fiber optics. b) Images of vortex arrays at different angular velocities ranging from 0.30 s^{-1} in image (a) to 0.59 s^{-1} in image (l). c) Vortex pattern in a dilute rotating BEC of sodium atoms (from (60)). The BEC was set in rotation by a laser stirring technique. After turning off the laser beams, the BEC was allowed to equilibrate for some time (~ms - s), then magnified by ballistic expansion before its density distribution was obtained by resonant absorption imaging. The axis of rotation is perpendicular to the image plane in b) and c). Typical distances between vortices are on the order of ~350 μm in He II and ~5 μm for the Na BEC.

While the experiments by Packard and co-workers provided a first direct visualization of vortex configurations in rotating He II, they also faced several complications that, ultimately, limited the amount of quantitative information gained from the studies (32; 63). In particular, vortex instabilities induced by mechanical disturbances were a limiting factor. Moreover, the experiments only imaged the terminal points

of the vortices at the liquid's surface, while their 3-dimensional shapes remained unknown. These limitations were only overcome more than a quarter century later, using an optical imaging approach.

Borrowing concepts from classical fluid dynamics experiments, techniques were developed based on *in situ* imaging of the spatial distribution of tracer particles. Micron-scale hydrogen clusters are particularly prominent tracers that form relatively stable suspensions in liquid He (33; 70-74). Fig. 3.2a shows the imaging experiment developed by Bewley, Lathrop, and Sreenivasan (75). Hydrogen tracer particles were created upon injection of an H_2:He gas mixture. After setting the cryostat in rotation and cooling LHe below T_λ, the tracers form an array of parallel lines with an areal density given by eq.(2.5) (Fig. 3.2b (28; 33)). This setup enabled significant advances including studies of extended rectilinear vortex lattices (33), the decay of vortex rings (76), as well as quantum turbulence (77; 78), Kelvin waves (79) and vortex reconnection events (80; 81). An example for the latter is shown in Fig. 3.2c (81).

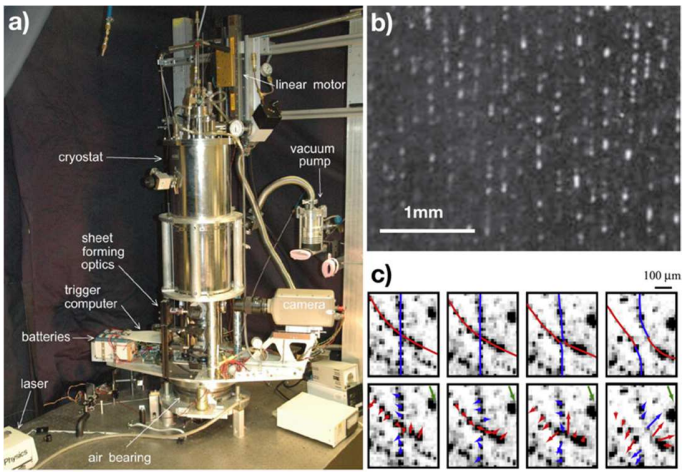

Figure 3.2: a) Vortex imaging inside a rotating cryostat. The entire apparatus resting on the air bearing is set in rotation, providing images of hydrogen tracer particles in the rotating frame (75). b) In the rotating superfluid, H_2 clusters align along vertical lines, tracing arrays of rectilinear vortices (33). c) Reconnection event between two vortices marked by red and blue lines in the upper row. Arrows in the lower row indicate tracer velocity vectors during the reconnection (81).

A drawback of the hydrogen tracer technique, however, is that it is difficult to extend towards much lower temperatures, thus interactions of the tracers with thermal excitations in the liquid influences the observed dynamics. The spatial resolution is also limited by the optical imaging approach. These limitations prompted further experimental developments, in particular, toward using X-ray scattering on nm sized tracer particles as outlined in sections 5-8.

Recently, the tracer technique has been applied to measure the velocity field of the normal component in He II (34; 82-84). Tracing by He_2* excimers enabled observation of turbulence in the normal component flow (83; 85; 86). However, tracing of single vortices by He_2* has not yet been demonstrated. Both the normal fluid component of He II as well as quantized vortices may impact the tracer motion and disentangling the different contributions is challenging (34; 84).

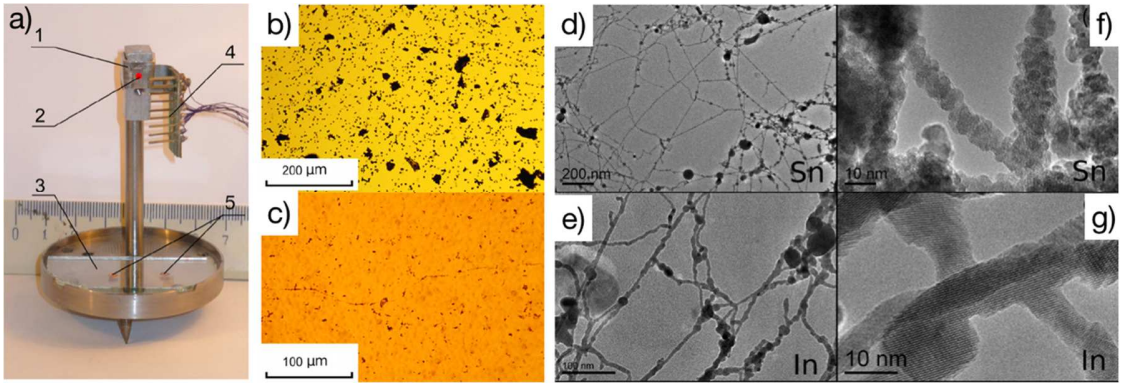

Figure 3.3: a) Laser ablation in liquid He: 1-metal foil target, 2-laser focus, 3-microscope slide, 4-electrode array, 5-TEM grids. The entire setup is placed in a liquid He bath (T=1.6 K) inside an optical cryostat and a laser beam is focused onto the metal target through the cryostat window. Voltages may be applied between adjacent electrodes both to study the impact of electric fields on the nanowire formation process as well as to study the electrical properties of nanowire networks under *in situ* and *ex situ* conditions. After laser exposure for ~minutes-hours, the microscope slide and TEM grids are removed and inspected by optical (b,c) and TEM (d-g) microscopy. Sediments deposited just below the target (b) and below the electrode array (c) exhibit different particle coverages and characteristic shapes with ~nm thin, ~mm long filaments appearing underneath the electrodes (87). TEM images reveal similar mesoscale nanowire network structures for Sn (d,f) and In (e,g) targets but with different crystalline sub-structures, suggesting different coagulation dynamics (88). The scale is shown in each panel.

Another class of experiments involves deposition of tracer particles on substrates that are studied by standard microscopy techniques after removal of the He liquid (87; 89). Figure 3.3a shows a setup developed by Gordon *et al.* to study nanowires created by laser ablation from metal targets in liquid He (87; 89; 90). Figures 3.3b and 3.3c show optical microscopy images of sediments deposited just below the target and underneath the electrode array, respectively. Higher-resolution TEM images of the latter (Fig. 3.3.d-g) reveal web-like networks of $\lesssim$10 nm diameter wires. The authors assign the formation of the nanostructures to growth inside vortices that attach to the pointed electrodes (87-90). However, laser ablation in the liquid He is a rather violent and highly complex process that produces a large variety of neutral and charged products (91; 92), which may result in the formation of various nanoparticles even in the absence of any vortices. The formation of metal nanowires is observed in experiments with both normal fluid and superfluid He. While the characteristic nanowire shapes and densities sometimes differ considerably for the two fluid phases (87), in some experiments they are virtually indistinguishable (89). Laser ablation experiments, therefore, are likely to have an impact in developing novel nanomaterials, for example, for nanocatalytic applications (87; 93) rather than studying vorticity in He II. Nevertheless, the concept of tracing vortices in He II by metal particles has provided important impulses for the study of vorticity in free He nanodroplets as will be described in more detail in section 5.

4. Shapes of spinning classical and superfluid droplets

Before proceeding to experiments on rotating superfluid droplets it is instructive to review rotation in classical viscous droplets. Starting with Newton, the equilibrium shapes of rotating astronomical bodies held together by gravitation have attracted great interest (94). It has been shown that the shapes of rotating liquid droplets held together by capillary forces belong to the same class of solutions and can serve as laboratory scale emulations of astronomical objects (95). The shapes of classical rotating droplets have been extensively studied theoretically (95-99) and experimentally (99; 100). The shape of a droplet executing rigid body rotation (RBR) is defined by the balance between capillary forces from surface tension and

centrifugal forces. The shape diagram for a rotating droplet is shown in Fig. 4.1a (95-99), and is described in terms of the reduced angular momentum, Λ, and reduced angular velocity, Ω, which are given by:

$$\Lambda = \frac{1}{\sqrt{8 \cdot \sigma \cdot \rho \cdot R^7}} \cdot L \quad , \qquad (4.1)$$

$$\Omega = \sqrt{\frac{\rho \cdot R^3}{8 \cdot \sigma}} \cdot \omega \quad . \qquad (4.2)$$

Here, L and ω are the angular momentum and angular velocity, respectively, in absolute units, σ is the surface tension of the liquid, ρ is its density, and R is the radius of a spherical droplet with the same volume as the distorted droplet. Droplets with different sizes but the same values of Λ and Ω have the same shape. Upon increasing Λ from zero, the equilibrium shape of a droplet evolves from spherical to oblate axially symmetric ($D_{\infty h}$), as indicated by the curve near the origin in Fig. 4.1. At $\Lambda \approx 1.2$ the curve branches. The upper $D_{\infty h}$ branch, shown as a dashed curve, is unstable with respect to quadrupole deformations. Stable shapes are described by the lower branch representing prolate droplets with D_{2h} symmetry that resemble triaxial ellipsoids for $1.2 < \Lambda < 1.5$, dumbbells for $\Lambda > 1.5$ and eventually become unstable against fission for $\Lambda > 2$. Unstable D_{3h}, D_{4h} and higher multipole paths that branch at higher Λ and Ω along the $D_{\infty h}$ curve are not shown in Fig. 4.1 (97). The numeric surface contours of the $D_{\infty h}$ and D_{2h} droplets at different Λ are presented in the Supplementary Material of reference (101). The droplet shapes can be characterized by the distances of the surface to the center along three mutually perpendicular directions: *a* is the distance along the rotational axis, *c* is the distance along the long axis perpendicular to *a*, whereas *b* is the intermediate distance along the axis perpendicular to the *a* and *c* axes (*c*=*b* in axially symmetric shapes). The droplet asymmetry is characterized by three aspect rations (AR) as shown in Fig. 4.1b (101).

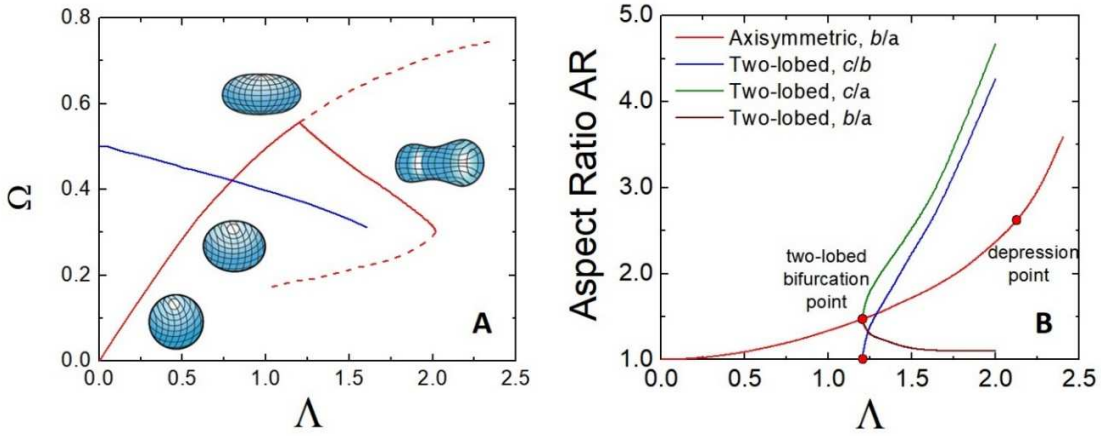

Fig. 4.1. A. Red curve: stability diagram for classical rotating droplets as a function of Ω, and Λ, see eqs. (4.1, 4.2). The upper branch corresponds to oblate axisymmetric shapes, whereas the lower branch to prolate two-lobed shapes. A calculated capillary wave branch is shown in blue (54). The bifurcation point is located at Λ = 1.2, Ω = 0.56 with AR = 1.48. B. AR, vs. Λ for classical axially symmetric oblate (red) and two-lobed prolate (green, blue, brown) droplet shapes. Reproduced from Ref. (101).

The study of equilibrium shapes of rotating superfluid droplets has only very recently become feasible (see sections 6, 7). RBR is not possible in a superfluid, which instead bears angular momentum through a collection of quantum vortices (28-31) or a potential flow (54; 102-104). Angular momentum can also be stored in the form of elementary excitations, such as phonons, rotons and ripplons, the contribution of which is small at the typical temperature T = 0.4 K in He droplets (15; 101). In the case of axially symmetric droplets at low T, the entire angular momentum is contained in vortices. In the limit of a large numbers of vortices, they arrange in an equilateral triangular lattice and, away from the vortex cores, produce velocity fields similar to those for RBR (28-31). For example, the shape of a rotating superfluid in a cylindrical container adopts a parabolic surface contour similar to that of a classically rotating liquid (29; 30; 105). Therefore, the shapes of rotating axisymmetric superfluid droplets are expected to resemble classical droplets rotating at the same ω, *L*. Some deviations have been predicted by DFT calculations for small droplets due to the relatively low number of vortices and surface effects (43). The situation is, however, more complex in prolate rotating superfluid droplets, where the angular momentum may stem from vortices as well as from capillary waves travelling along the droplet's equator. The latter imprint a

quadrupolar velocity field that is substantially different from that in RBR. Very recent DFT calculations (54) show that capillary waves produce a different branch in the Λ, Ω diagram and have a larger aspect ratio compared to classical prolate shapes for the same Λ, which is shown as a blue curve in Fig. 4.1. In classical droplets, capillary waves as well as vortices decay rapidly into RBR due to viscosity, but they may persist indefinitely in an isolated superfluid droplet. Therefore, the shapes of prolate superfluid droplets may differ significantly from their classical counterparts. Currently, the accurate shapes of prolate (and possibly higher order multipole) superfluid droplets remain to be discovered. One of the motivations for the X-ray and XUV scattering experiments described in sections 6 and 7 is to obtain the shapes of superfluid droplets and the corresponding vortex configurations at different angular momenta and in droplets of different sizes in order to assemble the stability diagram for superfluid droplets, such as that for classical droplets in Fig. 4.1.

5. *Ex situ* tracing of quantum vortices in He droplets

The availability of large helium droplets has created enticing new opportunities to study almost perfectly isolated, self-contained micro- and nano-scale superfluids (6; 9; 106). However, virtually none of the established methods for studying bulk superfluids can be applied to free droplets. Each droplet has a unique size, shape and state (L, ω) which can only be characterized by probing individual droplets (107; 108). While trapping of millimeter sized superfluid He drops by laser (109) and magnetic (110) fields has been achieved, corresponding studies of vorticity have not been reported. Attempts to detect vorticity in nanodroplets via spectroscopy on embedded molecules remained inconclusive (9). Instead, the first experimental evidence for the existence of quantized vortices in He droplets was provided by an *ex situ* imaging experiment of the Vilesov group (Fig. 5.1 (111)).

In the experiment, helium droplets with average diameters of 100-1000 nm containing, on average, $\langle N_{He} \rangle \approx 10^7$ - 2×10^{10} atoms were doped with ~10^3 - 10^6 Ag atoms (Fig. 5.1a). Downstream, the doped

droplet beam collided with substrates, which were then removed from the vacuum system and imaged by TEM. Figures 5.1b and 5.1c show characteristic Ag deposition patterns obtained for the smallest and largest droplets, respectively. While the small droplets produce round ~nm sized Ag patterns, deposition by large droplets leads to ~10 nm thin, ~500 nm long Ag filaments that consist of many separate or partially fused ~10 nm diameter clusters (Fig. 5.1d). The characteristic length of the filaments is comparable to the ~700 nm average diameter of the large doped droplets (111). The authors concluded that the filaments are produced via pinning of Ag atoms and clusters to quantum vortices inside the large droplets. It was hypothesized that liquid may acquire vorticity due to inhomogeneous flow and breakup of normal liquid inside the nozzle. The angular momentum is then transferred into superfluid vortices upon evaporative cooling of the droplets below T_λ in vacuum. The study was followed by a number of deposition experiments in other groups. Yang, Ellis and co-workers showed that the formation of nanowires in He droplets is a universal process (112). In addition to Ag (112), they produced nanowires from Ni, Cr, Au, and Si (112) as well as from sequentially added Ag and Si atoms (112).

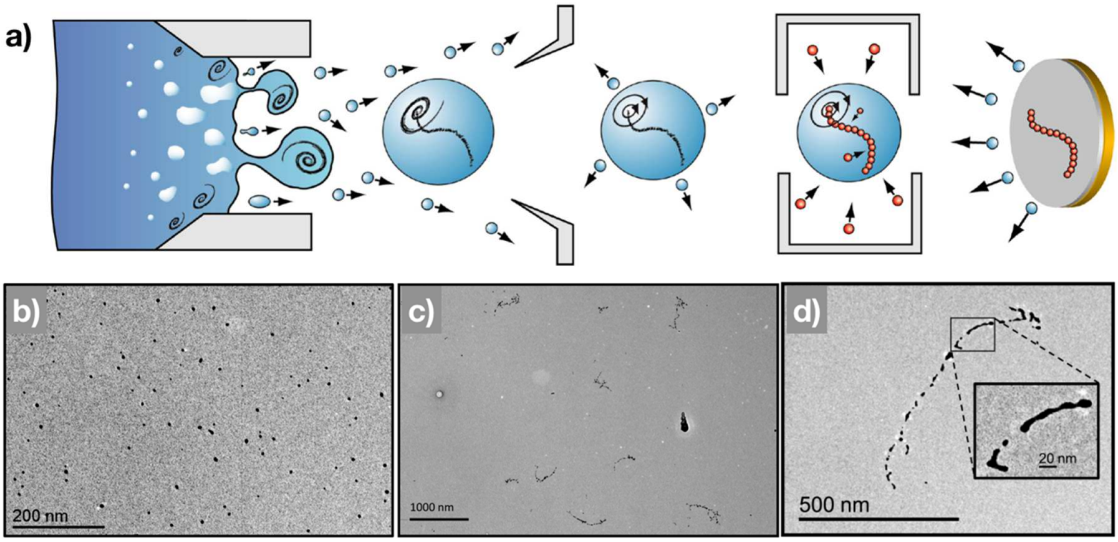

Figure 5.1: *Ex situ* imaging of vortices in He droplets. a) Droplets are generated by expanding liquid helium through a cryogenically cooled, micron size nozzle into vacuum and doped while passing through a hot pickup cell filled with Ag vapor. Upon impact of the doped droplets on a thin carbon film, the helium evaporates while the Ag structures formed inside the droplets remain attached to the substrate and are subsequently investigated by TEM. b) For ~100 nm diameter droplets, the deposition patterns are round. c) For droplets originally ~1 μm in diameter, the deposition patterns assume filament-like shapes, consistent with cluster pinning to quantum vortices. d) The magnified view of a single trace reveals a fragmented substructure (from (111)).

Understanding the effect of the droplet surface impact as well as reconstruction dynamics upon warm-up and transfer of the deposited structures to the TEM is a critical aspect in deposition experiments. The effects of surface diffusion on the deposited shapes has been studied in great detail in a series of experimental and theoretical investigations in the Ernst group (113-116). In Ref. (113) Ag deposits were kept at 77 K during deposition and transferred to a cryo-TEM in which the sample temperature could be varied between 77 K and 363 K. These studies were later extended to Au, Cu, and Ni nanowires, which were examined with ~1 nm resolution TEM at temperatures up to ~1600 K (114). As shown in Fig. 5.2a,e, the nanostructures have continuous, ramified structures when kept at sufficiently low temperatures. Such structures may result from fusing a large number of filaments produced on vortices. During the heating process, however, breakup into nanospheres and nanorods occurs. In particular, for Ag the transition takes place below room temperature, which explains the fragmented structures observed in previous deposition experiments (111; 112). The surface smoothing, breakup points, and fragment nanostructure contraction to

minimize the number of surface atoms are well reproduced by simulations using a 3D diffusion model as illustrated in Figures 5.2c,d and 5.2g,h (114; 116).

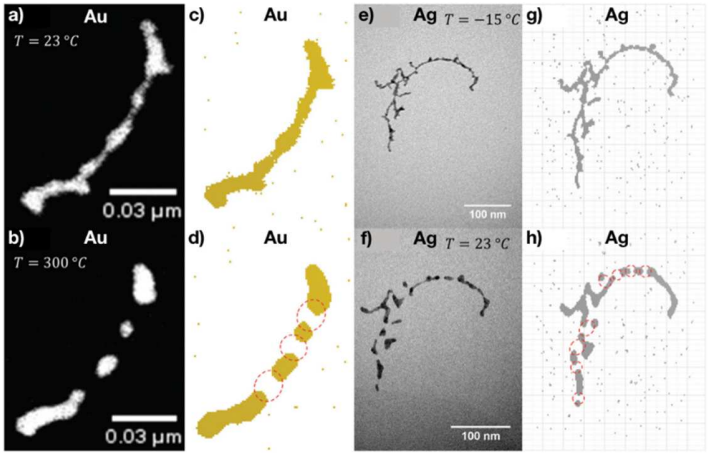

Figure 5.2: Measured (a,b,e,f) and simulated (c,d,g,h) metal dopant deposition patterns after soft landing of doped He droplets, illustrating the temperature dependent breakup of deposited nanostructures (from (114)). See text for details.

While the described surface reconstruction effects after deposition are experimentally accessible, the effect of the droplet impact on the initially deposited nanostructure morphologies is not. Thus, *ab initio* calculations have been developed to study the dynamics of the deposition (117-120). Comparison of classical trajectory (CT) and quantum mechanical TDDFT calculations describing the impact of a $^4He_{300}$ droplet on a rutile TiO_2(110)-(1×1) surface show distinct differences (117). Calculations for doped ^{4}He droplets with up to 10^5 He atoms and 5000 dopant atoms confirm soft landing processes for both Au atoms (119) and Ag clusters (120) with essentially unity sticking probability and a very limited impact of surface diffusion during the deposition process onto amorphous carbon substrates.

Dopant deposition techniques also provide a route to create unique, stable nanomaterials that cannot be obtained by any other means (13; 121; 122). The first Ag/Au and Ni/Au core-shell metal nanoparticles assembly in He droplets was demonstrated by Yan, Ellis and co-workers (123). Ernst and co-workers created Au/Ag and Ag/Au core-shell nanowires through sequential pickup of Au and Ag atoms by ~300

nm diameter droplets, and characterized them by element-specific nanoimaging techniques (124; 125). Lindsay and co-workers extended the method toward the creation of highly porous "cluster materials" (126-128), such as pre-reactive nanocomposites of magnesium and perfluoropolyether (PFPE). The work illustrated the potential of the deposition technique to create high energy density metal-oxidizer nano composites that are challenging to produce by other techniques due to their inherently high reactivity (127).

6. XUV and X-ray diffraction experiments

The *in situ* imaging of individual He nanodroplets and embedded particles has recently become possible through diffraction experiments that utilize radiation from XFELs and HHG light sources. Three characteristics of these light sources are critical for this advance: 1) The wavelengths are sufficiently short to resolve features as small as $\lesssim$20 nm (129; 130). 2) The pulses have a large enough flux ($\gtrsim 10^{18}$ photons/cm^2 for X-rays and $\gtrsim 10^{16}$ photons/cm^2 in the XUV) to generate a sufficient number of scattered photons (10^5) from the interaction of a single X-ray/XUV pulse with a single droplet. 3) The pulses are short enough ($\lesssim$100 fs) such that the scattering pattern is not blurred by droplet motion or destructive kinetics following the absorption of X-ray photons. Vilesov, Gessner, Bostedt and co-workers performed small-angle X-ray scattering experiments at the Linac Coherent Light Source (LCLS) XFEL at SLAC National Accelerator Laboratory to study free superfluid ^{4}He droplets containing ~10^8 to ~10^{11} atoms (diameters $D \approx$ 200-2000 nm) (108) (Fig. 6.1). In the experiment, ~100 fs long pulses with a repetition rate of 120 Hz and 1.5 keV photon energy intersected a continuous He droplet beam, resulting in a few scattering events per minute. It was found that the diffraction images of doped, micrometer-sized droplets often exhibit Bragg patterns consistent with aggregation of the Xe dopants on vortices that are arranged into triangular lattices (Fig. 6.1b,c). From the pattern in Fig. 6.1c, a vortex density of $n_V = 4.5 \times 10^{13}$ m^{-2} and, using eqn. (5), an angular velocity $\omega = 2.2 \times 10^6$ s^{-1} is derived.

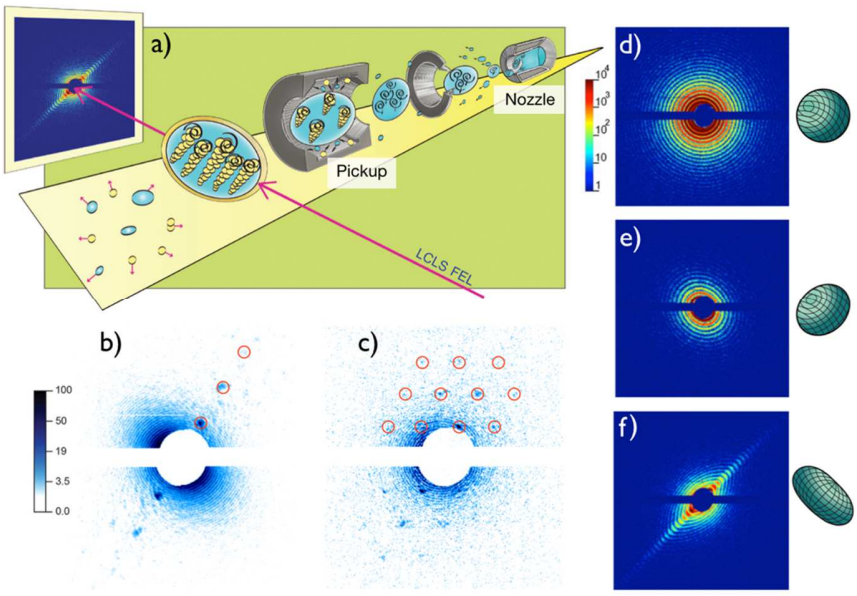

Figure 6.1: a) Single-shot X-ray diffraction experiment at LCLS XFEL. A beam of pure or Xe-doped He droplets is intersected by the XFEL beam and diffraction patterns of individual droplets are recorded. b),c) For doped droplets, Bragg patterns are observed, consistent with aggregation of Xe clusters in triangular vortex lattices. d)-f) Pure droplet diffraction patterns indicating both spherical (d) and centrifugally distorted (e,f) droplet shapes, which are illustrated in green (modified from (108)).

While many pure droplet scattering patterns are circular as expected from scattering off spherical objects (Fig. 6.1d), almost half of the patterns exhibit anisotropies of more than 6%, indicating that rotating droplets have large centrifugal distortion as illustrated by the green pictograms in Fig. 6.1. Some diffraction patterns exhibit aspect ratios up to 2.5 and pronounced intensity anomalies (streaks) as shown in Fig. 6.1f. The distorted patterns are well described by scattering simulations using shapes of classical rotating drops as discussed in section 4. For the streaked image in Fig. 6.1f, this analysis leads to an estimated angular velocity of $\omega = 1.4 \times 10^7\ s^{-1}$. Note that some of the vortex densities and angular velocities observed in free droplets are at least ~5 orders of magnitude larger than the ones observed in the rotating bucket experiments described in section 3 (32; 33). Some of the observed patterns were assigned to axially symmetric ($D_{\infty h}$) shapes with aspect ratios beyond the stability limit (AR=1.48) for two-lobed deformations (see section 4) (101; 108), in agreement with theoretical predictions (96).

The study was followed by significant activities to probe superfluid He droplets via ultrafast single-pulse diffraction (101; 129-132). Employing larger scattering angles compared to the first LCLS experiment, several groups confirmed the existence of prolate droplets belonging to the lower branch of the stability curve in Fig. 4.1A for large angular momenta (101; 131; 132). Wide-angle scattering contains more information about the three-dimensional shape of an object than small-angle scattering signals, which primarily represent the projection of the object on the detector plane. Figure 6.2a shows a diffraction pattern recorded by Vilesov and co-workers at the LCLS with two separate detectors, capturing extended small-angle scattering signals. The distinctly curved triple-streak is well reproduced by the simulation in Fig. 6.2b. It is based on the prolate triaxial droplet shape with a depression around the droplet waist displayed in Fig. 6.2c, which corresponds to a droplet with Λ=1.5 (101). Studies with longer XUV wavelengths yielded large number of diffraction images at wide scattering angles (131; 132). Figures 6.2d,e show two examples of streaked scattering patterns recorded by Rouzée and co-workers using an intense HHG light source operating simultaneously at four different wavelengths between ~47 and ~72 nm (131). The very pronounced curvature and overall structure of the scattering pattern Fig. 6.2e is captured well by the simulation in Fig. 6.2f that results from the biaxial prolate ("pill-shaped") droplet shown in the inset. Most recently, Möller and co-workers conducted an XUV diffraction experiment on pure He droplets at the FERMI XFEL using wavelengths between 32 and 65 nm (132). The wide-angle scattering experiments confirmed the existence of prolate triaxial rotating superfluid droplets with pill- and dumbbell-like shapes and, more generally, that the shapes of superfluid droplets resemble those of their classical counterparts.

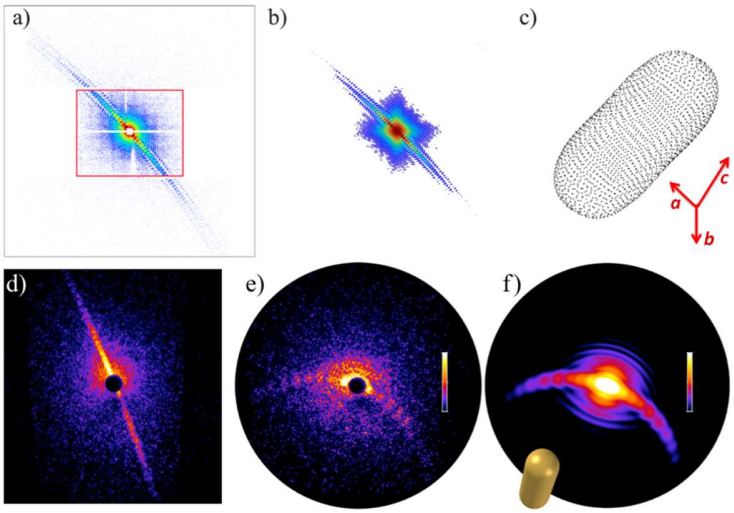

Figure 6.2: Observation of prolate rotating He droplets via wide-angle single-shot X-ray (a-c) (101) and XUV (d-f) (131) diffraction. a) Composite X-ray scattering pattern recorded at hν = 850 eV simultaneously with a small-angle (red rectangle) and a wide-angle (grey square) scattering detector at the LCLS, revealing a notably curved triple streak (scattering angles $\lesssim$10°). b) Simulated diffraction pattern for a triaxial prolate droplet pictured in c). d), e) Curved streaks from wide angle XUV diffraction using a HHG light source (h$\nu \approx$ 17 - 27 eV, scattering angles $\lesssim$40°). f) Simulated diffraction pattern of a biaxial prolate ("pill-shaped") droplet pictured in the inset.

Interestingly, no axisymmetric oblate shapes with aspect ratios beyond the classical stability limit were reported in either of the XUV diffraction studies (131; 132), in contrast to the LCLS experiments (101; 108). The discrepancy may be connected to the significantly different droplet generation conditions. More studies, however, are needed to consolidate the findings. We note that both XUV and X-ray light sources provide complementary opportunities and challenges. For example, the theoretical description of X-ray scattering by helium droplets is relatively straightforward as it falls within the Rayleigh-Gans-Debye approximation for scattering off optically thin objects (101; 108). This is not the case for studies in the XUV, where refraction is significant and which require more elaborate Mie scattering calculations (131). Principally, shorter wavelengths translate into a higher resolution limit, which can be relevant, for example, to resolve ~nm scale vortex tracer structures (see Section 7, (129; 130)). On the other hand, it is generally easier to record wide-angle scattering signals at longer wavelengths due to higher scattering efficiency. The

method of choice, therefore, depends on the goal of an experiment and, to a significant part, on the availability of a particular light source.

7. From diffraction patterns to droplet shapes and dopant density distributions

As illustrated in section 6, single-shot X-ray and XUV diffraction is a powerful tool to study shapes and vorticities of superfluid He droplets. At its core, the concept and its experimental implementation are very straightforward, essentially only requiring an intense, focused beam of pulsed light and a detector to record the scattering pattern. The key challenge, however, is to translate the recorded scattering patterns into real-space density distributions. The reconstruction of an object from its scattering pattern is referred to as coherent diffractive imaging (CDI) (133-141). For optically thin objects and small scattering angles, the complex amplitude of the scattered radiation corresponds to the two-dimensional (2D) Fourier transform (FT) of the projection of its density distribution onto the detector plane (101; 137; 138). Therefore, reconstructing the object density is principally possible through inverse FT of the scattering amplitude. However, the measured diffraction patterns only provide the moduli squared of the amplitude whereas the scattering phases are unknown. Thus, CDI requires the reconstruction of the missing phase information by iterative phase retrieval algorithms (133-138).

The fundamental assumption of CDI is that the missing phase information can be retrieved through oversampling of the scattering patterns (133-138). The availability of XFELs has spawned a flurry of activities in the field and we refer to corresponding reviews (139-141). So far, CDI has only been demonstrated for optically thin samples, which excludes refractive objects. For the specific case of doped helium droplets, Tanyag *et al.* developed an iterative phase retrieval algorithm that effectively uses the host droplet as a reference scatterer with a known scattering amplitude (129). Figure 7.1 outlines the concept of the droplet CDI (DCDI) method, which is based on a modified version of the error reduction algorithm (133).

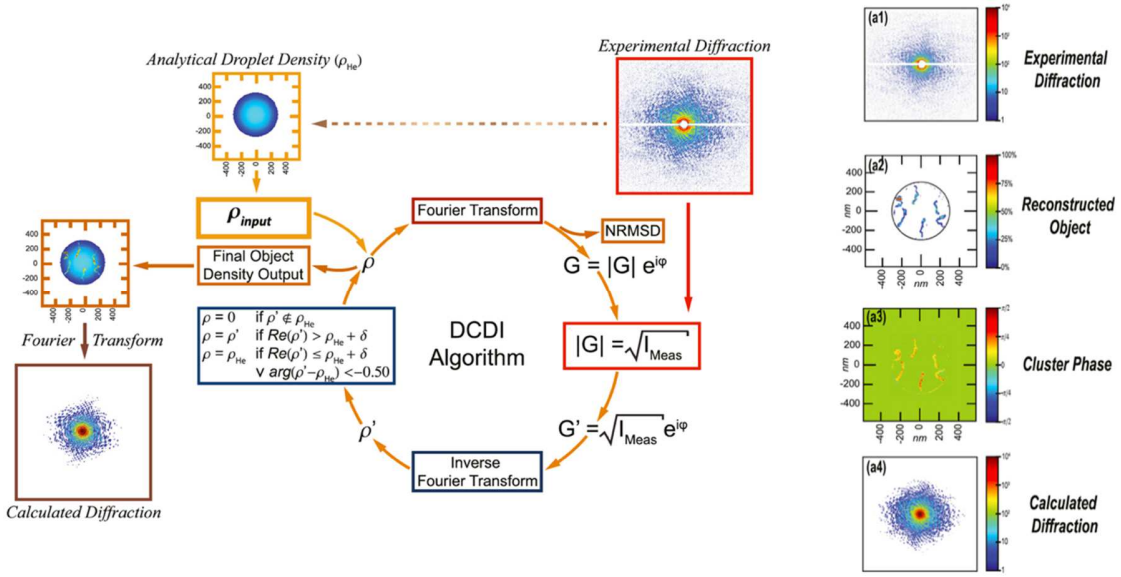

Figure 7.1: Left: Schematic of the DCDI algorithm. Right: Example diffraction data (a1), reconstructed sample densities (a2) and phases (a3) and calculated diffraction pattern (a4). The black circle in (a2) indicates the droplet boundary. See text for details (129).

DCDI takes advantage of the fact that the size and shape of host droplets can be derived from a central ring structure in the diffraction pattern even for doped droplets. The diffraction amplitude is then the sum of the known real amplitude from the droplet and the unknown (in general complex) amplitude from the dopants. The reconstruction is initiated by FT of the 2D projection of the droplet density distribution ρ(x,y), giving $G(x,y)=|G(x,y)| e^{i\varphi(x,y)}$. The modulus |G| of the FT is then replaced by the square root of the measured intensity I_{Meas} while the phase φ is retained, resulting in a modified scattering amplitude G'(x,y). Inverse FT of G' provides a first estimate of the combined density distribution ρ'(x,y) of droplet and dopants. This distribution is adjusted based on the known physical properties of the host-dopant system, imposing constraints such as that the dopants are inside the droplet's contour, that the dopant density exceeds the shot noise, δ, and positivity of the imaginary part of the density. Then, a new iteration of the FT/inverse FT cycle is initiated until the modulus |G| of the calculated scattering pattern has converged to

$\sqrt{I_{Meas}}$. Figure 7.1 shows an example including a measured (a1) and a calculated (a4) diffraction pattern along with the reconstructed density distribution (a2) and scattering phases (a3) of xenon clusters inside a ~600 nm diameter droplet, revealing a symmetric arrangement of six quantum vortices. The smallest reconstructed feature is ~18 nm across, which is comparable to the theoretical limit for the spatial resolution in small-angle CDI of $\approx \lambda/\theta_{max} \approx 12$ nm, where θ_{max} is the maximum scattering angle of the experimental diffraction patterns.

Fig. 7.1 a2 shows that the Xe density is concentrated within six filaments separated by about 100–200 nm. The formation of the filaments is consistent with the condensation of dopant atoms onto the cores of quantum vortices. The image in Fig. 2(a2) is consistent with an approximately hexagonal pattern of C-shaped filaments imaged at some angle with respect to the symmetry axis. It is evident that the filaments have kinks and exhibit an inhomogeneous density distribution. These effects may result from reconstruction of Xe filaments, whereby the van der Waals forces act to minimize the filament surface. Future studies should provide more details on the mechanism of the filaments' formation and reconstruction, in particular when molecular dopants are used.

Jones *et al.* employed the DCDI technique to study the spatial arrangements of Xe-doped vortices in small ($D \approx 200$ nm) helium droplets containing $\langle N_{He} \rangle \approx 10^8$ He atoms as illustrated in Figure 7.2 (130). The reconstructed Xe cluster densities (Fig. 7.2B2-F2) reveal symmetric arrangements of few vortices located close to the droplet surface and far away from each other. These observations deviate from DFT based predictions for vortex locations in pure droplets (43), which has been attributed to the impact of the Xe dopants on the rotational energy and angular momentum. A more detailed discussion of this effect is provided in section 8. The results also demonstrate that vorticity can have a dramatic impact on the distribution of dopants inside He nanodroplets. Prior to the XFEL experiments, He droplets were commonly modeled as isotropic, spherical objects with noble gas dopants located close to the center (142). The fact that the clusters can be found far away from the center (130) should be taken into account when modeling, for example, the interaction of reactive dopants or the synthesis of nanomaterials in He nanodroplets.

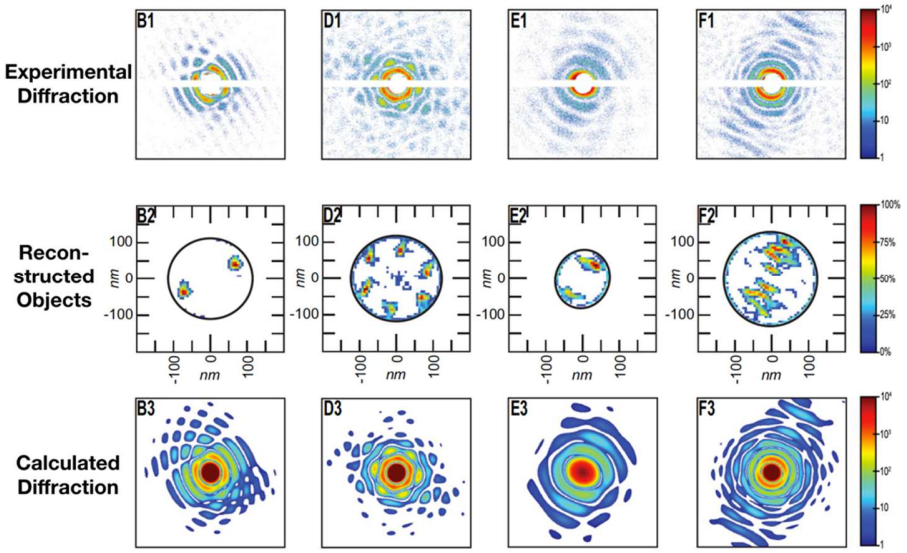

Figure 7.2: Few-vortex configurations (B2-F2) in ~200 nm diameter helium droplets, imaged by single-shot X-ray DCDI of Xe tracer particles (B1-F1). The black circles and ellipses indicate the droplet boundaries. The vortex axes are along the line of sight in B2,D2 and notably tilted in E2, F2. For comparison, B3-F3 show the calculated diffraction patterns of the reconstructed objects (130).

8. Effects of doping on vortex kinematics

The imaging of vortices in He nanodroplets relies on the decoration of vortex cores with clusters containing a large number of Xe atoms. This section presents a discussion of the impact of doping on the vortex coordinates, which is based on the model calculations presented in Ref. (143). We limit the discussion to a single vortex, the position of which is expected to be most sensitive to doping. In equilibrium, the doped vortices are stationary in a frame rotating with some angular velocity, ω. The equilibrium configuration of a doped vortex in a free droplet with total angular momentum

$$L = L_{vort} + L_{clust} \quad , \qquad (8.1)$$

is determined by minimizing the total energy

$$E = E_{vort} + E_{clust} + V_{solv} \, , \qquad (8.2)$$

where L_{vort} (E_{vort}) and L_{clust} (E_{clust}) are the angular momenta (kinetic energies) of the vortex and of the cluster revolving with the vortex, respectively. V_{solv} is the van der Waals solvation energy of the cluster in the He droplet (143). Some constraints regarding the vortex shape are inevitable in the model calculations (143). Analytic solutions for L_{vort} and E_{vort} are known for a rectilinear vortex in a cylinder (36; 38) and in a sphere (49), whereas the shape of undoped curved vortices may be obtained via numeric calculations (36; 37). It is convenient to present the discussion in terms of reduced quantities defined as:

$$r_r = \frac{r}{R},\ L_r = \frac{L}{L(0)},\ E_r = \frac{E}{E(0)} \text{ and } \omega_r = \frac{\omega}{\omega(0)},$$

where $L(0)$, $E(0)$ and $\omega(0)$ are values for a rectilinear vortex at the center of the droplet and r is the minimum distance between the vortex and the rotational axis. For a bare vortex in an R = 100 nm droplet: $L(0)$ = 8.9 × 10^7 ħ, $E(0)$ = 1.1×10^4 K and $\omega(0)$ = 1.08 10^7 rad s^{-1}. Fig. 8.1 shows the calculated values for r_r, E_r and ω_r versus L_r for an R=100 nm droplet containing a single curved vortex. Different curves are for bare and doped vortices decorated with experimentally feasible numbers of Xe atoms arranged into filaments of radii R_{Xe} as indicated (143).

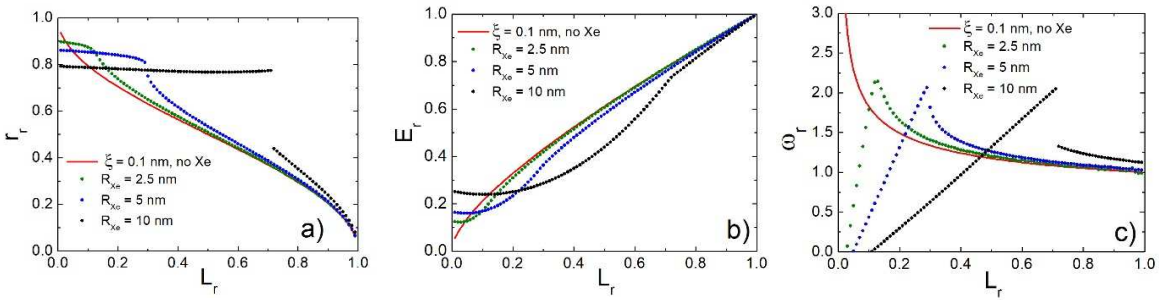

Fig. 8.1. Theoretical estimates of (a) reduced equilibrium position r_r, (b) reduced energy E_r, and (c) reduced angular velocity ω_r as a function of the reduced angular momentum L_r for a curved quantum vortex in a spherical droplet with R_{He} = 100 nm, containing N_{He} = 8.9 × 10^7 helium atoms. The results for a bare vortex (ξ= 0.1 nm) are shown in red. The results for curved vortices with R_{Xe}=2.5 nm, 5 nm and 10 nm filaments containing 3.4×10^4, 1.4×10^5, and 5.4×10^5 Xe atoms are shown by green, blue and black dots, respectively. Reproduced with permission from Ref. (143).

Fig. 8.1 a) shows that, with decreasing L_r, a bare vortex moves away from the center, until it reaches the surface of the droplet where it annihilates at $L_r = 0$. The presence of Xe atoms leads to an increase of r_r for most values of L_r that can be ascribed to a centrifugal force on the vortex. For the narrowest Xe filament (R_{Xe} = 2.5 nm), the curves for r_r, E_r and ω_r closely follow those for the bare vortex until the doped vortex reaches the surface region. Upon increase of the filament diameter (mass), the curves exhibit pronounced discontinuities. In particular, the R_{Xe} = 10 nm solution bifurcates to the surface region for $L_r < 0.7$, while the E_r and ω_r solutions exhibit pronounced slope discontinuities. These trends indicate a transition from kinematics dominated by the vortex in the interior of the droplets to those determined by the solvation potential and rotational energy of the Xe filament close to the surface. In the surface region, the angular velocity of a bare vortex increases rapidly, whereas ω_r of a doped vortex decreases and even becomes negative at small L_r. Solutions with negative ω_r are metastable, whereas the stable solution corresponds to a revolving filament without a vortex (143).

The results of the model calculations indicate that the positions of doped vortices in axially symmetric droplets can be used to characterize their rotational state (143). Vortex locations away from the surface region with r_r less than ~0.8 may be used to estimate the droplet's rotational energy, total angular momentum, and angular velocity. However, when Xe clusters are found in the surface region, the system is dominated by the kinetic energy and solvation potential of the dopants, and the kinematic parameters cannot be deduced from the positions of the clusters with reasonable accuracy.

9. Conclusions and Outlook

Superfluid helium provides unique opportunities to study the similarities and differences between quantum mechanical and classical phenomena in macroscopic systems. The study of rotational motion and fluid shapes has long played an important role in this respect. The recently developed capability to image shapes and vorticities of individual helium nanodroplets has created new possibilities to investigate

quantum hydrodynamics in free, isolated, self-contained systems in new regimes of rotational excitation and with vanishingly small external perturbations. Within only a few years, the traditional perception of He nanodroplets as perfectly homogeneous, isotropic, spherical objects that may be challenging to set in rotation has been replaced by a much more diverse picture. Droplets exhibit angular momenta ranging from negligible to $\approx 100\hbar$ per atom with corresponding shapes varying from spheres and spheroids (101; 108) rotating relatively slowly to dumbbells (101; 131; 132) on the verge of disintegration due to centrifugal forces. In oblate biaxial droplets, the angular momentum is stored in multiple quantum vortices that are arranged in symmetrical configurations such as triangular lattices (108; 129; 130). The combined effect of vortices and capillary waves on the droplet shape, as discussed in section 4.1, is still to be explored. One may speculate that the interplay between quantum vortices and capillary waves (which are not damped in superfluids) may yield shapes not attainable in classical drops.

Currently, it is not possible to make a direct comparison between the shapes of classical and superfluid droplets, because both angular momenta and angular velocities are estimated from the shapes. It would be desirable to simultaneously determine droplet shapes and corresponding vortex configurations, which will yield L and ω. Such measurements would allow to generate $\Omega - \Lambda$ correlation diagrams for superfluid droplets, such as the ones for classical droplets shown in Fig. 4.1, revealing similarities and differences between classical and quantum rotation. The origins of the droplets' rotational excitation during the jet expansion should be further studied and possibly used to create advanced sources with sharper droplet size- and angular momentum-distributions. For example, nozzles with longer channels operating at $T < T_\lambda$ may be used to study quantum turbulence (51-53; 77; 78; 86). In order to gain a better understanding of the impact of vortices on rotating He droplet shapes, future experiments will be extended to ^{3}He nanodroplets. ^{3}He droplets remain normal fluid under typical experimental conditions, providing an opportunity to study similarities and differences between rotating superfluid and normal fluids under almost identical conditions.

An extension of these studies to mixed ^{3}He-^{4}He droplets presents another frontier. At $T < 0.87$ K, a phase separation occurs into a nearly pure ^{3}He phase on the droplet surface and a ^{4}He rich phase in its

interior (144). The morphology of the phases in rotating droplets is still to be discovered. In addition, the mechanism of phase separation has been extensively discussed for several decades. Proposed mechanisms include quantum tunneling and vortex-assisted phase separation (145). Classical low-temperature experiments cannot yield a definitive answer due to the relatively slow rate of temperature change achievable in a conventional cryostat and the correspondingly small level of supersaturation. The evaporative cooling rate of droplets can reach 10^6 K/s, opening an opportunity to study real-time kinetics and underlying mechanisms of the phase separation.

Imaging of doped helium nanodroplets has demonstrated several new opportunities for fundamental studies of superfluid hydrodynamics and their application as a cryogenic matrix. DCDI has been employed to map quantum vortices containing Xe clusters with ~20 nm resolution (129; 130). The studies revealed a significant impact of doping on the vortex locations (130). A natural extension of these studies will be the imaging of vortex constellations in larger doped droplets as well as in prolate or two-lobed He droplets. More generally, the DCDI technique may be utilized for *in situ* microscopy studies on a diverse range of nano-clusters.

The aggregation of particles inside liquid helium is not only instrumental for the detection of vortices but also intriguing in its own right (146). The unhindered motion of foreign particles and efficient dissipation of the heat of formation renders He droplets unique cryogenic “test tubes” for aggregation experiments close to absolute zero temperature. At ambient temperatures, aggregation usually evolves toward structures characterized by a global minimum in the free energy landscape. At low temperatures, however, inter-particle interactions dominate, whereas entropic effects are negligible. Therefore, weak intermolecular orientation forces, such as dipole-dipole (147), or hydrodynamic attraction by quantum vortices, play a significant role during the approach of particles, yielding unusual structures, such as atomically thin chains(147) or fractals (146). On the other hand, aggregation in ^{3}He droplets devoid of vortices may be used to study low-temperature aggregation in a perfectly isotropic liquid. DCDI provides a route to study the structure and formation dynamics of such aggregates in great detail, potentially enabling routes to synthesize novel nanomaterials.

Whether for the study of superfluidity in finite droplets, quantum nucleation, low-temperature chemistry, or for applications of rotating, superfluid nano-labs in materials synthesis, the recent advances in helium nanodroplet imaging techniques have created exciting new opportunities awaiting to be explored by experiments and theory alike. A relatively small number of studies by only a few groups has significantly enhanced our understanding of quantum vorticity and rotational motion in nanoscale superfluid droplets. The expansion of these early studies toward a much larger range of topics will greatly benefit from the fast pace at which laboratory- and accelerator-based ultrafast XUV- and X-ray light sources are currently being developed and implemented. The basic techniques have been demonstrated, they are ready to be exploited and expanded by a growing community.

Acknowledgments

O.G. was supported by the U.S. Department of Energy, Office of Science, Office of Basic Energy Sciences, Chemical Sciences, Geosciences and Biosciences Division, through Contract No. DE-AC02-05CH11231. A.F.V. was supported by NSF Grants No. DMR-1701077 and CHE-1664990.

References:

1. Toennies JP, Vilesov AF. 1998. Spectroscopy of atoms and molecules in liquid helium. *Annu Rev Phys Chem* 49:1-41
2. Callegari C, Lehmann KK, Schmied R, Scoles G. 2001. Helium Nanodroplet Isolation Rovibrational Spectroscopy: Methods and Recent Results. *J. Chem. Phys.* 115:10090-110
3. Northby JA. 2001. Experimental studies of helium droplets. *The Journal of Chemical Physics* 115:10065-77
4. Stienkemeier F, Vilesov AF. 2001. Electronic spectroscopy in He droplets. *The Journal of Chemical Physics* 115:10119-37
5. Toennies JP, Vilesov AF, Whaley KB. 2001. Superfluid helium droplets: An ultracold nanolaboratory. *Phys Today* 54:31-7
6. Toennies JP, Vilesov AF. 2004. Superfluid helium droplets: A uniquely cold nanomatrix for molecules and molecular complexes. *Angew Chem Int Edit* 43:2622-48
7. Barranco M, Guardiola R, Hernandez ES, Mayol R, Navarro J, Pi M. 2006. Helium nanodroplets: an overview. *J. Low Temp. Phys.* 142:1-81

8. Choi MY, Douberly GE, Falconer TM, Lewis WK, Lindsay CM, et al. 2006. Infrared spectroscopy of helium nanodroplets: novel methods for physics and chemistry. *Int. Rev. Phys. Chem.* 25:15-75
9. Stienkemeier F, Lehmann KK. 2006. Spectroscopy and Dynamics in Helium Nanodroplets. *J Phys B-at Mol Opt* 39:R127-R66
10. Tiggesbäumker J, Stienkemeier F. 2007. Formation and Properties of Metal Clusters Isolated in Helium Droplets. *Phys Chem Chem Phys* 9:4748-70
11. Callegari C, Ernst WE. 2011. Helium Droplets as Nanocryostats for Molecular Spectroscopy—from the Vacuum Ultraviolet to the Microwave Regime. In *Handbook of High-resolution Spectroscopy.*, ed. M Quack, F Merkt:1551-94. Chichester: John Wiley & Sons, Ltd. Number of 1551-94 pp.
12. Kuyanov-Prozument K, Skvortsov D, Slipchenko M, Sartakov BG, Vilesov AF, eds. 2011. *Matrix isolation spectroscopy in helium droplets*. Singapore: Pan Stanford Publishing. 203-30 pp.
13. Yang SF, Ellis AM. 2013. Helium droplets: a chemistry perspective. *Chem Soc Rev* 42:472-84
14. Mudrich M, Stienkemeier F. 2014. Photoionisaton of pure and doped helium nanodroplets. *Int Rev Phys Chem* 33:301-39
15. Tanyag RM, Jones CF, Bernando C, O'Connell SMO, Verma D, Vilesov AF. 2018. Experiments with Large Superfluid Helium Nanodroplets. In *Cold Chemistry: Molecular Scattering and Reactivity Near Absolute Zero*, ed. A Osterwalder, O Dulieu:389-443. Cambridge: Royal Society of Chemistry. Number of 389-443 pp.
16. Ancilotto F, Barranco M, Coppens F, Eloranta J, Halberstadt N, et al. 2017. Density functional theory of doped superfluid liquid helium and nanodroplets. *Int. Rev. Phys. Chem.* 36:621–707
17. Ziemkiewicz MP, Neumark DM, Gessner O. 2015. Ultrafast electronic dynamics in helium nanodroplets. *Int Rev Phys Chem* 34:239-67
18. Lemeshko M, Schmidt R. 2017. Molecular impuruties interacting with many-particle environment: From ultracold gases to helium nanodroplets. In *Cold Chemistry: Molecular Scattering and Reactivity Near Absolute Zero*, ed. A Osterwalder, O Dulieu:444-95. Cambridge: Royal Society of Chemistry. Number of 444-95 pp.
19. Hartmann M, Miller RE, Toennies JP, Vilesov A. 1995. Rotationally resolved spectroscopy of SF_6 in liquid-helium clusters - a molecular probe of cluster temperature. *Phys Rev Lett* 75:1566-9
20. Grebenev S, Hartmann M, Havenith M, Sartakov B, Toennies JP, Vilesov AF. 2000. The rotational spectrum of single OCS molecules in liquid ^{4}He droplets. *J. Chem. Phys.* 112:4485-95
21. Grebenev S, Toennies JP, Vilesov AF. 1998. Superfluidity within a small helium-4 cluster: The microscopic Andronikashvili experiment. *Science* 279:2083-6
22. McKellar ARW, Xu YJ, Jäger W. 2006. Spectroscopic exploration of atomic scale superfluidity in doped helium nanoclusters. *Physical Review Letters* 97:183401-1-4
23. Pentlehner D, Nielsen JH, Slenczka A, Mølmer K, Stapelfeldt H. 2013. Impulsive Laser Induced Alignment of Molecules Dissolved in Helium Nanodroplets. *Physical Review Letters* 110:093002-1-5
24. Christiansen L, Nielsen JH, Pentlehner D, Underwood JG, Stapelfeldt H. 2015. Alignment enhancement of molecules embedded in helium nanodroplets by multiple laser pulses. *Physical Review A* 92:053415-1-6
25. Lemeshko M. 2017. Quasiparticle Approach to Molecules Interacting with Quantum Solvents. *Physical Review Letters* 118:095301-1-5
26. Chatterley AS, Shepperson B, Stapelfeldt H. 2017. Three-Dimensional Molecular Alignment Inside Helium Nanodroplets. *Physical Review Letters* 119:073202-1-5
27. Landau LD. 1941. The Theory of Superfluidity of Helium II. *J. Phys. (Moscow)* 5:185-204

28. Feynman RP. 1955. Application of quantum mechanics to liquid helium. In *Progress in Low Temperature Physics*, ed. CJ Gorter, 1:1-53. Amsterdam: North-Holland Publishing Company. Number of 1-53 pp.
29. Tilley DR, Tilley J. 1990. *Superfluidity and Superconductivity*. Bristol: Institute of Physics Publ.
30. Donnelly RJ. 1991. *Quantized Vortices in Helium II*. Cambridge: Cambridge University Press
31. Pitaevskii L, Stringari S. 2016. *Bose-Einstein Condensation and Superfluididty*. Oxford: Oxford University Press. 553 pp.
32. Yarmchuk EJ, Gordon MJV, Packard RE. 1979. Observation of Stationary Vortex Arrays in Rotating Superfluid-Helium. *Physical Review Letters* 43:214-7
33. Bewley GP, Lathrop DP, Sreenivasan KR. 2006. Superfluid helium - Visualization of quantized vortices. *Nature* 441:588
34. Paoletti MS, Fiorito RB, Sreenivasan KR, Lathrop DP. 2008. Visualization of Superfluid Helium Flow. *J. Phys. Soc. Jpn.* 77:111007-1-7
35. Vinen WF. 1961. Detection of Single Quanta of Circulation in Liquid Helium II. *Proc R Soc Lon Ser-A* 260:218-36
36. Bauer GH, Donnelly RJ, Vinen WF. 1995. Vortex Configurations in a Freely Rotating Superfluid Drop. *J Low Temp Phys* 98:47-65
37. Lehmann KK, Schmied R. 2003. Energetics and possible formation and decay mechanisms of vortices in helium nanodroplets. *Physical Review B (Condensed Matter and Materials Physics)* 68:224520-1-10
38. Hess GB. 1967. Angular Momentum of Superfluid Helium in a Rotating Cylinder. *Phys Rev* 161:189-93
39. Dalfovo F, Mayol R, Pi M, Barranco M. 2000. Pinning of quantized vortices in helium drops by dopant atoms and molecules. *Physical Review Letters* 85:1028-31
40. Sadd M, Chester GV, Reatto L. 1997. Structure of a vortex in superfluid He-4. *Physical Review Letters* 79:2490-3
41. Reif F, Meyer L. 1960. Study of superfluidity in liquid He by ion motion. *Phys. Rev.* 119:1164-73
42. Donnelly RJ, Barenghi CF. 1998. The Observed Properties of Liquid Helium at the Saturated Vapor Pressure. *J Phys Chem Ref Data* 27:1217-74
43. Ancilotto F, Pi M, Barranco M. 2015. Vortex arrays in nanoscopic superfluid helium droplets. *Physical Review B (Condensed Matter and Materials Physics)* 91:100503(R)-1-5
44. Mateo D, Eloranta J, Williams GA. 2015. Interaction of ions, atoms, and small molecules with quantized vortex lines in superfluid ^{4}He. *J Chem Phys* 142:064510-1-9
45. Ancilotto F, Pi M, Barranco M. 2014. Vortex arrays in a rotating superfluid ^{4}He nanocylinder. *Phys Rev B* 90:174512-1-8
46. Pshenichnyuk IA, Berloff NA. 2016. Inelastic scattering of xenon atoms by quantized vortices in superfluids. *Physical Review B (Condensed Matter and Materials Physics)* 94:184505-1-8
47. Coppens F, Ancilotto F, Barranco M, Halberstadt N, Pi M. 2017. Capture of Xe and Ar atoms by quantized vortices in ^{4}He nanodroplets. *Phys.Chem.Chem.Phys.* 19:24805-18
48. Campbell LJ, Ziff RM. 1979. Vortex Patterns and Energies in a Rotating Superfluid. *Phys Rev B* 20:1886-902
49. Nam ST, Bauer GH, Donnelly RJ. 1996. Vortex patterns in a freely rotating superfluid. *J Korean Phys Soc* 29:755-64
50. Schwarz KW. 1985. 3-Dimensional Vortex Dynamics in Superfluid He-4 - Line-Line and Line-Boundary Interactions. *Phys Rev B* 31:5782-804
51. Hanninen R, Baggaley AW. 2014. Vortex filament method as a tool for computational visualization of quantum turbulence. *P Natl Acad Sci USA* 111:4667-74

52. Adachi H, Fujiyama S, Tsubota M. 2010. Steady-state counterflow quantum turbulence: Simulation of vortex filaments using the full Biot-Savart law. *Phys Rev B* 81:104511-1-7
53. Yui S, Tsubota M. 2015. Counterflow quantum turbulence of He-II in a square channel: Numerical analysis with nonuniform flows of the normal fluid. *Phys Rev B* 91:184504-1-12
54. Ancilotto F, Barranco M, Pi M. 2018. Spinning superfluid ^{4}He droplets. *Physical Review B (Condensed Matter and Materials Physics)* 97:184515-1-5
55. Karn PW, Starks DR, Zimmermann W. 1980. Observation of Quantization of Circulation in Rotating Superfluid He-4. *Phys Rev B* 21:1797-805
56. Rayfield GW, Reif F. 1963. Evidence for The Creation and Motion of Quantized Vortex Rings in Superfluid Helium. *Physical Review Letters* 11:305-8
57. Rayfield GW, Reif F. 1964. Quantized Vortex Rings in Superfluid Helium. *Phys Rev* 136:A1194-A208
58. Careri G, McCormick WD, Scaramuzzi F. 1962. Ions in rotating liquid helium II. *Phys. Lett.* 1:61-3
59. Douglass RL. 1964. Ion Trapping in Rotating Helium II. *Physical Review Letters* 13:791-4
60. Abo-Shaeer JR, Raman C, Vogels JM, Ketterle W. 2001. Observation of vortex lattices in Bose-Einstein condensates. *Science* 292:476-9
61. Packard RE, Sanders TM. 1969. Detection of Single Quantized Vortex Lines in Rotating He II. *Physical Review Letters* 22:823-6
62. Packard RE, Sanders TM. 1972. Observations on Single Vortex Lines in Rotating Superfluid Helium. *Physical Review A* 6:799-807
63. Williams GA, Packard RE. 1974. Photographs of Quantized Vortex Lines in Rotating He II. *Physical Review Letters* 33:280-3
64. Grimes CC, Adams G. 1992. Infrared-absorption spectrum of the electron bubble in liquid helium. *Phys Rev B* 45:2305-10
65. Rosenblit M, Jortner J. 1995. Dynamics of the Formation of an Electron Bubble in Liquid Helium. *Physical Review Letters* 75:4079-82
66. Abrikosov AA. 1957. On the Magnetic Properties of Superconductors of the Second Group. *Sov. Phys. JETP-USSR* 5:1174
67. Tkachenko VK. 1966. Stability of Vortex Lattices. *Sov. Phys. JETP-USSR* 23:1049
68. Matthews MR, Anderson BP, Haljan PC, Hall DS, Wieman CE, Cornell EA. 1999. Vortices in a Bose-Einstein condensate. *Physical Review Letters* 83:2498-501
69. Fetter AL. 2009. Rotating trapped Bose-Einstein condensates. *Rev Mod Phys* 81:647-91
70. Chopra KL, Brown JB. 1957. Suspension of Particles in Liquid Helium. *Phys Rev* 108:157-
71. Craig PP, Pellam JR. 1957. Observation of Perfect Potential Flow in Superfluid. *Phys Rev* 108:1109-12
72. Koehler TR, Pellam JR. 1962. Observation of Torque Exerted by Pure Superflow. *Phys Rev* 125:791-4
73. Chung DY, Critchlow PR. 1965. Motion of Suspended Particles in Turbulent Superflow of Liquid Helium II. *Physical Review Letters* 14:892-4
74. Kitchens TA, Steyert WA, Taylor RD, Craig PP. 1965. Flow Visualization in He II: Direct Observation of Helmholtz Flow. *Physical Review Letters* 14:942-5
75. Bewley GP. 2006. *Using frozen hydrogen particles to observe rotating and quantized flows in liquid helium*. Yale University
76. Bewley GP, Sreenivasan KR. 2009. The Decay of a Quantized Vortex Ring and the Influence of Tracer Particles. *J Low Temp Phys* 156:84-94
77. Paoletti MS, Fisher ME, Sreenivasan KR, Lathrop DP. 2008. Velocity Statistics Distinguish Quantum Turbulence from Classical Turbulence. *Physical Review Letters* 101:154501-1-4

78. Barenghi CF, Skrbek L, Sreenivasan KR. 2014. Introduction to quantum turbulence. *PNAS* 111:4647-52
79. Fonda E, Meichle DP, Ouellette NT, Hormoz S, Lathrop DP. 2014. Direct observation of Kelvin waves excited by quantized vortex reconnection. *PNAS* 111:4707-10
80. Bewley GP, Paoletti MS, Sreenivasan KR, Lathrop DP. 2008. Characterization of reconnecting vortices in superfluid helium. *PNAS* 105:13707-10
81. Paoletti MS, Fisher ME, Lathrop DP. 2010. Reconnection dynamics for quantized vortices. *Physica D: Nonlinear Phenomena* 239:1367-77
82. Zhang T, Sciver SWV. 2005. Large-scale turbulent flow around a cylinder in counterflow superfluid ^{4}He. *Nature Physics* 1:36-8
83. Guo W, Mantia ML, Lathrop DP, Sciver SWV. 2014. Visualization of two-fluid flows of superfluid helium-4. *PNAS* 111:4653-8
84. Mastracci B, Guo W. 2018. Exploration of thermal counterflow in He II using particle tracking velocimetry. *Phys. Rev. Fluids* 3:063304-1-17
85. Guo W, Wright JD, Cahn SB, Nikkel JA, McKinsey DN. 2009. Metastable Helium Molecules as Tracers in Superfluid 4He. *Physical Review Letters* 102:235301-1-4
86. Gao J, Guo W, Yui S, Tsubota M, Vinen WF. 2018. Dissipation in quantum turbulence in superfluid ^{4}He above 1 K. *Phys Rev B* 97:184518-1-10
87. Gordon EB, Karabulin AV, Matyushenko VI, Sizov VD, Khodos II. 2012. The role of vortices in the process of impurity nanoparticles coalescence in liquid helium. *Chem Phys Lett* 519-20:64-8
88. Gordon EB, Karabulin AV, Matyushenko VI, Sizov VD, Khodos II. 2012. The electrical conductivity of bundles of superconducting nanowires produced by laser ablation of metals in superfluid helium. *Appl. Phys. Lett.* 101:052605
89. Lebedev V, Moroshkin P, Grobety B, Gordon E, Weis A. 2011. Formation of Metallic Nanowires by Laser Ablation in Liquid Helium. *J Low Temp Phys* 165:166-76
90. Gordon EB, Karabulin AV, Matyushenko VI, Sizov VD, Khodos II. 2010. Electric properties of metallic nanowires obtained in quantum vortices of superfluid helium. *Low Temperature Physics* 36:590-5
91. Gordon EB, Kulish MI, Karabulin AV, Matyushenko VI. 2017. Non-isothermal physical and chemical processes in superfluid helium. *Low Temperature Physics* 43:1086-93
92. Yang GW. 2007. Laser ablation in liquids: Applications in the synthesis of nanocrystals. *Progress in Materials Science* 52:648-98
93. Gordon EB, Karabulin AV, Morozov AA, Matyushenko VI, Sizov VD, Khodos II. 2014. Structure and Properties of Platinum, Gold and Mercury Nanowires Grown in Superfluid Helium. *J. Phys. Chem. Lett.* 5:1072-6
94. Chandrasekhar S. 1967. Ellipsoidal Figures of Equilibrium - an Historical Account. *Commun. Pur. Appl. Math.* 20:251-67
95. Cohen S, Plasil F, Swiatecki WJ. 1974. Equilibrium Configurations of Rotating Charged or Gravitating Liquid Masses with Surface-Tension. 2. *Ann Phys-New York* 82:557-96
96. Chandrasekhar S. 1965. The stability of a rotating liquid drop. *Proc. Roy. Soc. London A* 286:1-26
97. Brown RA, Scriven LE. 1980. The Shape and Stability of Rotating Liquid-Drops. *P Roy Soc Lond a Mat* 371:331-57
98. Butler SL, Stauffer MR, Sinha G, Lilly A, Spiteri RJ. 2011. The shape distribution of splash-form tektites predicted by numerical simulations of rotating fluid drops. *J. Fluid Mech.* 667:358-68
99. Baldwin KA, Butler SL, Hill RJA. 2015. Artificial tektites: an experimental technique for capturing the shapes of spinning drops. *Sci Rep-Uk* 5:7660-1-5
100. Hill RJA, Eaves L. 2008. Nonaxisymmetric Shapes of a Magnetically Levitated and Spinning Water Droplet. *Physical Review Letters* 101:234501-1-4

101. Bernando C, Tanyag RM, Jones C, Bacellar C, Bucher M, et al. 2017. Shapes of rotating superfluid helium nano-droplets. *Physical Review B (Condensed Matter and Materials Physics)* 95:064510
102. Seidel GM, Maris HJ. 1994. Morphology of Superfluid Drops with Angular-Momentum. *Physica B* 194:577-8
103. Whitaker DL, Weilert MA, Vicente CL, Maris HJ, Seidel GM. 1998. Oscillations of charged helium II drops. *J Low Temp Phys* 110:173-8
104. Fetter AL. 1974. Vortex nucleation in deformed rotating cylinders. *J. Low Temp. Phys.* 16:532-55
105. Andronikashvili EL, Mamaladze YG. 1967. Chapter III Rotation of Helium II. In *Progress in Low Temperature Physics*, ed. CJ Gorter, 5:79-160: Elsevier. Number of 79-160 pp.
106. Becker EW, Klingelhöfer R, Lohse P. 1961. Strahlen aus kondensiertem Helium im Hochvakuum. *Z. Naturforsch.* 16a:1259
107. Gomez LF, Loginov E, Sliter R, Vilesov AF. 2011. Sizes of large He droplets. *The Journal of Chemical Physics* 135:154201-1-9
108. Gomez LF, Ferguson KR, Cryan JP, Bacellar C, Tanyag RMP, et al. 2014. Shapes and Vorticities of Superfluid Helium Nanodroplets. *Science* 345:906-9
109. Weilert MA, Whitaker DL, Maris HJ, Seidel GM. 1995. Laser levitation of superfluid helium. *J Low Temp Phys* 98:17-35
110. Weilert MA, Whitaker DL, Maris HJ, Seidel GM. 1996. Magnetic Levitation and Noncoalescence of Liquid Helium. *Physical Review Letters* 77:4840-3
111. Gomez LF, Loginov E, Vilesov AF. 2012. Traces of Vortices in Superfluid Helium Droplets. *Physical Review Letters* 108:155302-1-5
112. Spence D, Latimer E, Feng C, Boatwright A, Ellis AM, Yang S. 2014. Vortex-induced aggregation in superfluid helium droplets. *Phys Chem Chem Phys* 16:6903-6
113. Volk A, Knez D, Thaler P, W. Hauser A, Grogger W, et al. 2015. Thermal instabilities and Rayleigh breakup of ultrathin silver nanowires grown in helium nanodroplets. *Phys Chem Chem Phys*:24570-5
114. Schnedlitz M, Lasserus M, Knez D, Hauser AW, Hofer F, Ernst WE. 2017. Thermally induced breakup of metallic nanowires: experiment and theory. *Phys Chem Chem Phys* 19:9402-8
115. Thaler P, Volk A, Ratschek M, Koch M, Ernst WE. 2014. Molecular dynamics simulation of the deposition process of cold Ag-clusters under different landing conditions. *The Journal of Chemical Physics* 140:044326-1-9
116. Hauser AW, Schnedlitz M, Ernst WE. 2017. A coarse-grained Monte Carlo approach to diffusion processes in metallic nanoparticles. *Eur. Phys. J. D* 71:150-1-8
117. Aguirre NF, Mateo D, Mitrushchenkov AO, Pi M, de Lara-Castells MP. 2012. Helium mediated deposition: Modeling the He−TiO2(110)-(1×1) interaction potential and application to the collision of a helium droplet from density functional calculations. *The Journal of Chemical Physics* 136:124703-1-14
118. Lara-Castells MPd, Stoll H, Civalleri B, Causà M, Voloshina E, et al. 2014. Communication: A combined periodic density functional and incremental wave-function-based approach for the dispersion-accounting time-resolved dynamics of 4He nanodroplets on surfaces: 4He/graphene. *The Journal of Chemical Physics* 141:151102-1-5
119. de Lara-Castells MP, Aguirre NF, Stoll H, Mitrushchenkov AO, Mateo D, Pi M. 2015. Communication: Unraveling the 4He droplet-mediated soft-landing from ab initio-assisted and time-resolved density functional simulations: Au@4He300/TiO2(110). *The Journal of Chemical Physics* 142:131101
120. Fernández-Perea R, Gómez LF, Cabrillo C, Pi M, Mitrushchenkov AO, et al. 2017. Helium Droplet-Mediated Deposition and Aggregation of Nanoscale Silver Clusters on Carbon Surfaces. *J. Phys. Chem. C* 121:22248-57

121. Mozhayskiy V, Slipchenko MN, Adamchuk VK, Vilesov AF. 2007. Use of helium nanodroplets for assembly, transport, and surface deposition of large molecular and atomic clusters. *The Journal of Chemical Physics* 127:094701-1-6
122. Wu Q, Ridge CJ, Zhao S, Zakharov D, Cen J, et al. 2016. Development of a New Generation of Stable, Tunable, and Catalytically Active Nanoparticles Produced by the Helium Nanodroplet Deposition Method. *J. Phys. Chem. Lett.* 7:2910-4
123. Boatwright A, Feng C, Spence D, Latimer E, Binns C, et al. 2013. Helium droplets: a new route to nanoparticles. *Faraday Discuss.* 162:113-24
124. Thaler P, Volk A, Lackner F, Steurer J, Knez D, et al. 2014. Formation of bimetallic core-shell nanowires along vortices in superfluid He nanodroplets. *Phys Rev B* 90:155442-1-5
125. Haberfehlner G, Thaler P, Knez D, Volk A, Hofer F, et al. 2015. Formation of bimetallic clusters in superfluid helium nanodroplets analysed by atomic resolution electron tomography. *Nat Commun* 6:9779-1-6
126. Emery SB, Rider KB, Little BK, Schrand AM, Lindsay CM. 2013. Magnesium cluster film synthesis by helium nanodroplets. *The Journal of Chemical Physics* 139:054307-1-6
127. Emery SB, Rider KB, Lindsay CM. 2014. Stabilized Magnesium/Perfluoropolyether Nanocomposite Films by Helium Droplet Cluster Assembly. *Propellants, Explosives, Pyrotechnics* 39:161-5
128. Emery SB, Xin Y, Ridge CJ, Buszek RJ, Boatz JA, et al. 2015. Unusual behavior in magnesium-copper cluster matter produced by helium droplet mediated deposition. *The Journal of Chemical Physics* 142:084307
129. Tanyag RMP, Bernando C, Jones CF, Bacellar C, Ferguson KR, et al. 2015. Communication: X-ray coherent diffractive imaging by immersion in nanodroplets. *Struct. Dyn.* 2:051102-1-9
130. Jones CF, Bernando C, Tanyag RMP, Bacellar C, Ferguson KR, et al. 2016. Coupled motion of Xe clusters and quantum vortices in He nanodroplets. *Phys Rev B* 93:180510(R)-1-6
131. Rupp D, Monserud N, Langbehn B, Sauppe M, Zimmermann J, et al. 2017. Coherent diffractive imaging of single helium nanodroplets with a high harmonic generation source. *Nat Commun* 8:493
132. Langbehn B, Sander K, Ovcharenko Y, Peltz C, Clark A, et al. 2018. Three-dimensional shapes of spinning helium nanodroplets. *arXiv:1802.10584v2 [physics.atm-clus]*
133. Fienup JR. 1982. Phase retrieval algorithms: a comparison. *Appl. Opt., AO* 21:2758-69
134. Miao J, Sayre D, Chapman HN. 1998. Phase retrieval from the magnitude of the Fourier transforms of nonperiodic objects. *J. Opt. Soc. Am. A* 15:1662-9
135. Miao J, Charalambous P, Kirz J, Sayre D. 1999. Extending the methodology of X-ray crystallography to allow imaging of micrometre-sized non-crystalline specimens. *Nature* 400:342-4
136. Marchesini S, He H, Chapman HN, Hau-Riege SP, Noy A, et al. 2003. X-ray image reconstruction from a diffraction pattern alone. *Phys Rev B* 68:140101(R)-1-4
137. Chapman HN, Barty A, Marchesini S, Noy A, Hau-Riege SP, et al. 2006. High-resolution ab initio three-dimensional x-ray diffraction microscopy. *J. Opt. Soc. Am. A* 23:1179-200
138. Marchesini S. 2007. Invited Article: A unified evaluation of iterative projection algorithms for phase retrieval. *Review of Scientific Instruments* 78:011301
139. Barty A, Küpper J, Chapman HN. 2013. Molecular Imaging Using X-Ray Free-Electron Lasers. *Annual Review of Physical Chemistry* 64:415-35
140. Chapman HN, Nugent KA. 2010. Coherent lensless X-ray imaging. *Nat Photon* 4:833-9
141. Miao J, Ishikawa T, Robinson IK, Murnane MM. 2015. Beyond crystallography: Diffractive imaging using coherent x-ray light sources. *Science* 348:530-5
142. Lehmann KK. 1999. Potential of a neutral impurity in a large ^{4}He cluster. *Mol. Phys.* 97:645-66

143. Bernando C, Vilesov AF. 2018. Kinematics of the Doped Quantum Vortices in Superfluid Helium Droplets. *J. Low.Temp. Phys.* 191:242-56
144. Dobbs ER. 2001. *Helium Three*. Oxford, New York: Oxford University Press. 1086 pp.
145. Barranco M, Guilleumas M, Jezek DM, Lombard RJ, Navarro J, Pi M. 1999. Nucleation in Dilute ^{3}He-^{4}He Liquid Mixtures at Low Temperatures. *J Low Temp Phys* 117:81-100
146. Alves SG, Vilesov AF, Ferreira SC. 2009. Effects of the mean free path and slippery in a model for the aggregation of particles in superfluid media. *J. Chem. Phys.* 130:244506-1-6
147. Nauta K, Miller RE. 1999. Nonequilibrium Self-Assembly of Long Chains of Polar Molecules in Superfluid Helium. *Science* 283:1895-7